Phase dynamics in an AC-driven multiterminal Josephson junction analog

François Amet ●,[1,*] Sara Idris,[1] Aeron McConnell ●,[1] Brian Opatosky ●,[1] and Ethan Arnault[2,1]

[1]*Department of Physics and Astronomy, Appalachian State University, Boone, North Carolina 28607, USA*
[2]*Department of Physics, Duke University, Durham, North Carolina 27708, USA*

In the presence of an AC drive, multiterminal Josephson junctions exhibit the inverse AC Josephson effect, where the oscillations of the superconducting phase of each junction can lock onto one another or onto the external drive. The competition between these different phase-locked states results in a complex array of quantized voltage plateaus whose stability strongly depend on the circuit parameters of the shunted junctions. This phase diagram cannot be explored with low-temperature transport experiments alone, given the breadth of the parameter space, so we present an easily tunable analog circuit whose dynamical properties emulate those of a three-terminal junction. We focus on the observation of the multiterminal inverse AC Josephson effect, and we discuss how to identify Shapiro steps associated with each of the three junctions as well as their quartet states. We only observe integer phase-locked states in strongly overdamped networks, but fractional Shapiro steps appear as well when the quality factor of the junctions increases. Finally, we discuss the role of transverse coupling in the synchronization of the junctions.

I. INTRODUCTION

In a multiterminal junction, a Josephson coupling is established between multiple superconducting electrodes across a common normal channel. Those devices recently attracted considerable interest [1–7] because of the energy spectrum of their Andreev bound states. Indeed these states, which result from the Andreev reflections of charge carriers at each superconducting interface, have an energy spectrum that can emulate artificial band structures with interesting topological features such as Weyl points and non-Abelian monopoles [8–15].

While the quantum effects in these devices provide unique opportunities, the dynamical effects of these circuits can give rise to unexpected effects [16–19]. This is because the time evolution of the superconducting phases obey nonlinear differential equations that are comparable to those of driven coupled pendulums [20–24]. As a result, many features that are traditionally recognized as quantum effects in Josephson junctions, may actually be caused by the nonlinearity of the equations describing them. For instance, fractional Shapiro steps, which are often attributed to the nonsinusoidal current phase relation (CPR) of a device, can actually be observed in two or three-terminal junctions with a strictly sinusoidal CPR as a consequence of the classical equations governing them [4,25]. Another example arises in three-terminal devices, where supercurrent resonances can occur when commensurate finite voltages are applied to each terminal. While those have been attributed to Andreev multiplets entangling four or more electrons, they can in fact have a strictly dynamical interpretation which is observable in classical systems [23,26]. Therefore, as a way to distinguish quantum causes from classical ones, there is a need to realize an experimental platform that mimics the dynamical processes in these devices, decoupled from any complicating quantum effects.

In the case of single junctions, analog circuits based on voltage-controlled oscillators (VCO) can be designed so that the voltage at one of their nodes follows the same differential equation as the junction phase in the resistively and capacitively shunted junction (RCSJ) model [25,27–30]. Recently, we showed how a broad range of RCSJ phenomena could be observed in such a circuit [25]. These include hysteretic switching, activated escape rate caused by thermal-noise, phase-locking, and chaos. Furthermore, the design allowed the observation of the time evolution of the phase itself, as well as its frequency spectrum. These are not experimentally observable in standard junctions, because the phase dynamics occur on subnanosecond timescales.

In this work, we expand these results to the case of a three-terminal junction. We designed an analog circuit that follows the same dynamical system as a network of three shunted junctions. The high tunability of this circuit allows us to not only replicate recent observations made on ballistic multiterminal junctions, but also to explore their vast parameter space more conveniently than with real devices. We first show how to identify transitions between phase-locked states associated with each of the three junctions. Additionally, we observe synchronization phenomena involving two junctions and the drive. These result in Shapiro steps which have yet to be observed in real devices, along so-called "quartet resonances" at quantized values of $pV_i + qV_j$, where $V_{i,j}$ are junction voltages. Finally, we show how an increase in the quality factor favors the stabilization of fractional Shapiro steps, and we analyze their dynamics.
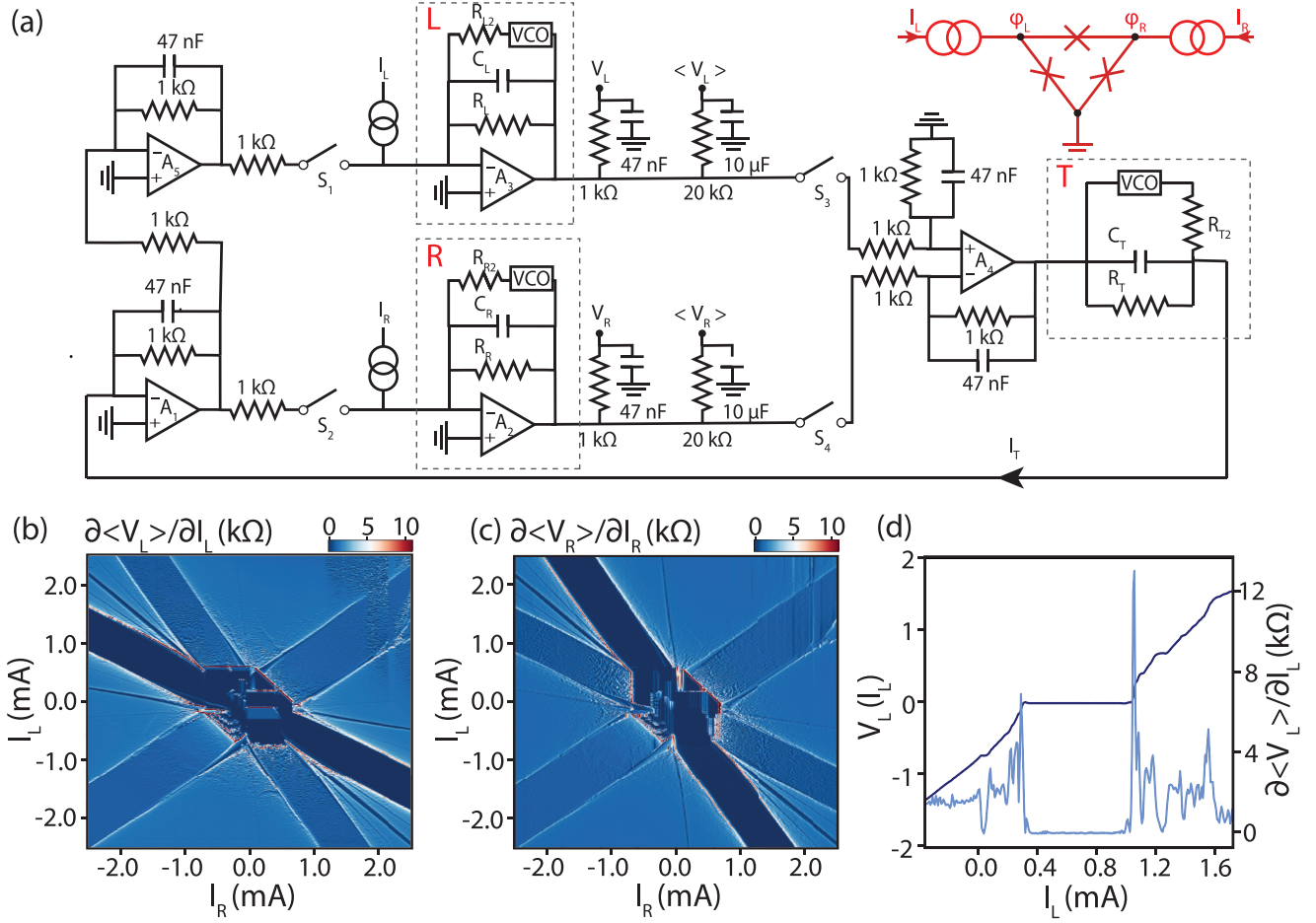
---
*ametf@appstate.edu

FIG. 1. (a) Schematic of the analog circuit used in this work. In red is a schematic of an equivalent three-terminal network of Josephson junctions. The bottom superconducting contact is grounded and its phase set as zero. Subcircuits corresponding to the left (L), right (R), and transverse junctions (T) are highlighted with dashed boxes. (b) Effective differential resistance of the circuit $\partial\langle V_L\rangle/\partial I_L$ as a function of the two biases I_L and I_R. (c) Effective differential resistance of the circuit $\partial\langle V_R\rangle/\partial I_R$ as a function of the two biases I_L and I_R. (d) Cross section of $\langle V\rangle_L(I_L)$ for $I_R = -1.47$ mA.

II. THE THREE-TERMINAL SHUNTED JUNCTION MODEL

We model the three-terminal Josephson junction by the network which is sketched in red in Fig. 1(a). The left and right terminals are respectively labeled L and R, and the bottom contact is grounded, so its phase can be assumed to be zero. Each junction is assumed to be shunted by a resistor and a capacitor. Applying Kirchhoff laws at each node, we find [31]

$$\frac{\hbar}{2e}\mathcal{C}\ddot{\Phi} + \frac{\hbar}{2e}\mathcal{G}\dot{\Phi} + I_c(\Phi) = I.$$

Here,

$$\Phi = \begin{pmatrix} \varphi_L \\ \varphi_R \end{pmatrix} \quad \text{and} \quad I = \begin{pmatrix} I_L \\ I_R \end{pmatrix}$$

are two-row vectors, and we defined the following quantities:

$$I_c(\Phi) = \begin{pmatrix} I_L\sin(\varphi_L) + I_T\sin(\varphi_L - \varphi_R) \\ I_R\sin(\varphi_R) + I_T\sin(\varphi_R - \varphi_L) \end{pmatrix},$$

$$\mathcal{C} = \begin{pmatrix} C_L + C_T & -C_T \\ -C_T & C_L + C_T \end{pmatrix},$$

$$\mathcal{G} = \begin{pmatrix} G_L + G_T & -G_T \\ -G_T & G_L + G_T \end{pmatrix}.$$

$I_c(\Phi)$ depends on the current phase relations of the junctions, which for simplicity are assumed to be sinusoidal.

The circuit shown in black on Fig. 1(a) reproduces the same system of differential equations as the three-terminal network of Josephson junctions. A simpler circuit analog of a two-terminal Josephson junction was already studied in Ref. [25] and is here generalized to the three-terminal case. It relies on three home-made voltage-controlled oscillators (VCOs), which have been simplified as box diagrams for clarity but are shown in the Supplemental Material [31]. These oscillators deliver an output sine-wave of amplitude α and frequency kV, where V is the input voltage of the VCO and k its voltage to frequency gain.

If we define $\dot{\varphi}_L$ and $\dot{\varphi}_R$ as the output voltages of operation amplifiers A3 and A2 (multiplied by $2\pi k$), we show in the Supplemental Material [31] that Φ verifies the equivalent differential equation:

$$\frac{1}{2\pi k}\mathcal{C}\ddot{\Phi} + \frac{1}{2\pi k}\mathcal{G}\dot{\Phi} + I_c(\Phi) = I.$$

It is thus possible to monitor the time evolution of output voltages of A2 and A3 and get insights into the phase dynamics of three-terminal Josephson junctions. Here, we defined the two vector I as

$$I = \begin{pmatrix} -I_L \\ -I_R \end{pmatrix}.$$

III. DC TRANSPORT CHARACTERIZATION

We first evaluate the switching properties of the analog Josephson junction network in the presence of a DC bias. Figures 1(b) and 1(c) show the effective differential resistances $\partial\langle V_L\rangle/\partial I_L$ and $\partial\langle V_R\rangle/\partial I_R$ as a function of DC biases I_L and I_R.

The maps draw strong similarities with previous work on three-terminal junctions shown in Refs. [3,5,6]. Three arms of suppressed differential resistance correspond to each of the three junctions being in the zero-voltage state. The strongest resonances of suppressed differential resistance correspond to $V_L = 0$, $V_R = 0$, and $V_L - V_R$. The maps of those voltages are shown in the Supplemental Material [31].

A cross section of the differential resistance $\partial\langle V_L\rangle/\partial I_L$ as a function of I_L is shown in light blue in Fig. 1(d). The corresponding I-V curve $V_L(I_L)$ is shown in darker blue on the same plot. Those cross sections are strongly reminiscent of typical Josephson junction transport, and evidently the region of suppressed differential resistance correspond to a plateau at $V_L = 0$.

In addition to the three main zero-voltage resonances, the maps 1(b) and 1(c) show additional resonances along contours defined as $p\langle V_L\rangle + q\langle V_R\rangle = 0$ with p, $q \in \mathbb{N}$. Those resonances are also seen on the cross sections 1(d) around $I_L \approx 0$ and $I_L \approx 1.25$ mA. These correspond to classical realization of Andreev multiplet states and were the focus of a different publication [23].

IV. INTEGER PHASE LOCKING

We now turn to the transport properties of the network in the presence of an AC drive. Conventional multiterminal Josephson junctions can exhibit the multiterminal inverse AC Josephson effect in the presence of microwave radiation [4]. In the presence of a periodic drive, the junction phase can lock onto a multiple of the drive frequency $n\omega$ [32], which results in a quantized voltage across the junction. This is a purely dynamical effect, which can thus be replicated in a Josephson junction analog, as shown in Ref. [25]. Here, the three analog junction frequencies are on the order of 500 Hz. It is therefore possible to observe phase-locking in the presence of an AC excitation provided by a simple function generator.

We first characterize the inverse AC Josephson effect when the coupling between the Josephson junctions is disconnected [using the switches shown in Fig. 1(a)]. Here the three analog junctions have a quality factor of about 0.3 and are thus over-damped. We observe Shapiro steps in $\langle V_L\rangle(I_L)$ and $\langle V_R\rangle(I_R)$, shown in Figs. 2(a) and 2(b). The voltage quanta are f_{ac}/k, where k is the voltage to frequency gain of the VCO. Similar to the conventional Josephson junction case, the height of the voltage steps is expected to be proportional to the AC drive frequency f_{ac}. For each junction, we thus plot the normalized output voltage at two different frequencies and find that the quantization indeed scales with f_{ac}.

We can then determine the evolution of the width of the Shapiro steps as a function of the amplitude of the AC drive. In the case of a voltage biased Josephson junction, that width can be determined analytically and follows Bessel-like oscillations as a function of the drive amplitude. While this is not the case in current-biased junctions, oscillations are still observed and can be perfectly replicated within the RCSJ model [25]. Figure 2(c) shows that trend: dark blue regions correspond to a vanishing differential resistance $\partial\langle V_L\rangle/\partial I_L$ and therefore quantized Shapiro steps in the I-V curve of the junction. This map is typical of overdamped behavior, as observed in both standard junctions [33] and analog junctions [25].

Now that signatures of phase locking in uncoupled analog junctions are established, we restore the transverse coupling and determine the evolution of the differential resistances $\partial\langle V_L\rangle/\partial I_L$ and $\partial\langle V_R\rangle/\partial I_R$ as a function of both biases [Figs. 2(d) and 2(e)]. Important patterns in the data are sketched in Fig. 2(f). Shapiro plateaus are observed in both channels and they correspond to the darkest blue stripes observed in Figs. 2(d) and 2(e). Plateaus of constant $\langle V_L\rangle$ in Fig. 2(d) are sketched as dark red lines in 2(f), whereas plateaus of constant $\langle V_R\rangle$ in Fig. 2(e) are sketched as dark blue lines in 2(f). We also label the index n of the Shapiro step (such that $V = n\frac{f_{ac}}{k}$). Note that the overall slopes of the plateaus are identical to the contours $\langle V_L\rangle = 0$ and $\langle V_R\rangle = 0$ in the DC regime, which are shown in Ref. [31]. In Fig. 2(d), the imprint of the $\langle V_R\rangle$ plateaus is observed as slightly lighter blue stripes. This is because the sudden drop in $\langle V_R\rangle$ causes the effective resistance from the left contact to ground to drop slightly because of the resistor network connecting the junctions. Similarly, plateaus of constant $\langle V_L\rangle$ affect $\langle V_R\rangle$ and are visible as light-blue stripes in Fig. 2(e). The transverse junction can also become phase locked. When this happens, $\langle V_L - V_R\rangle$ is quantized, which forms plateaus parallel to the contour $\langle V_L - V_R\rangle = 0$ in the DC regime. These correspond to diagonal stripes spanning the map from the bottom left to the top right corner [sketched in pink in Fig. 2(f)].

Finally, we observe that classical quartet states also yield Shapiro steps, although these are fainter, which are visible on both maps. The most noticeable correspond to plateaus of quantized $\langle V_L + V_R\rangle$ and quantized $\langle 2V_L - V_R\rangle$ and are sketched in light blue in Fig. 2(f). Voltage steps are observed whenever $pV_l + qV_r = \frac{f_{ac}}{k}$, with $(p, q) = (1, 1)$ and $(2, -1)$. For a true Josephson junction network, this would correspond to $pV_l + qV_r = \frac{hf_{ac}}{2e}$. In Ref. [23], we showed how finite supercurrents at $pV_l + qV_r = 0$ do not necessarily come from entangled pairs of Cooper pairs but can instead be dynamically stabilized by a process reminiscent of Kapitza's inverted pendulum problem. Here, we see that in the presence of an AC bias, those resonances result in Shapiro steps where two phases are synchronized and locked to the drive. Hints of
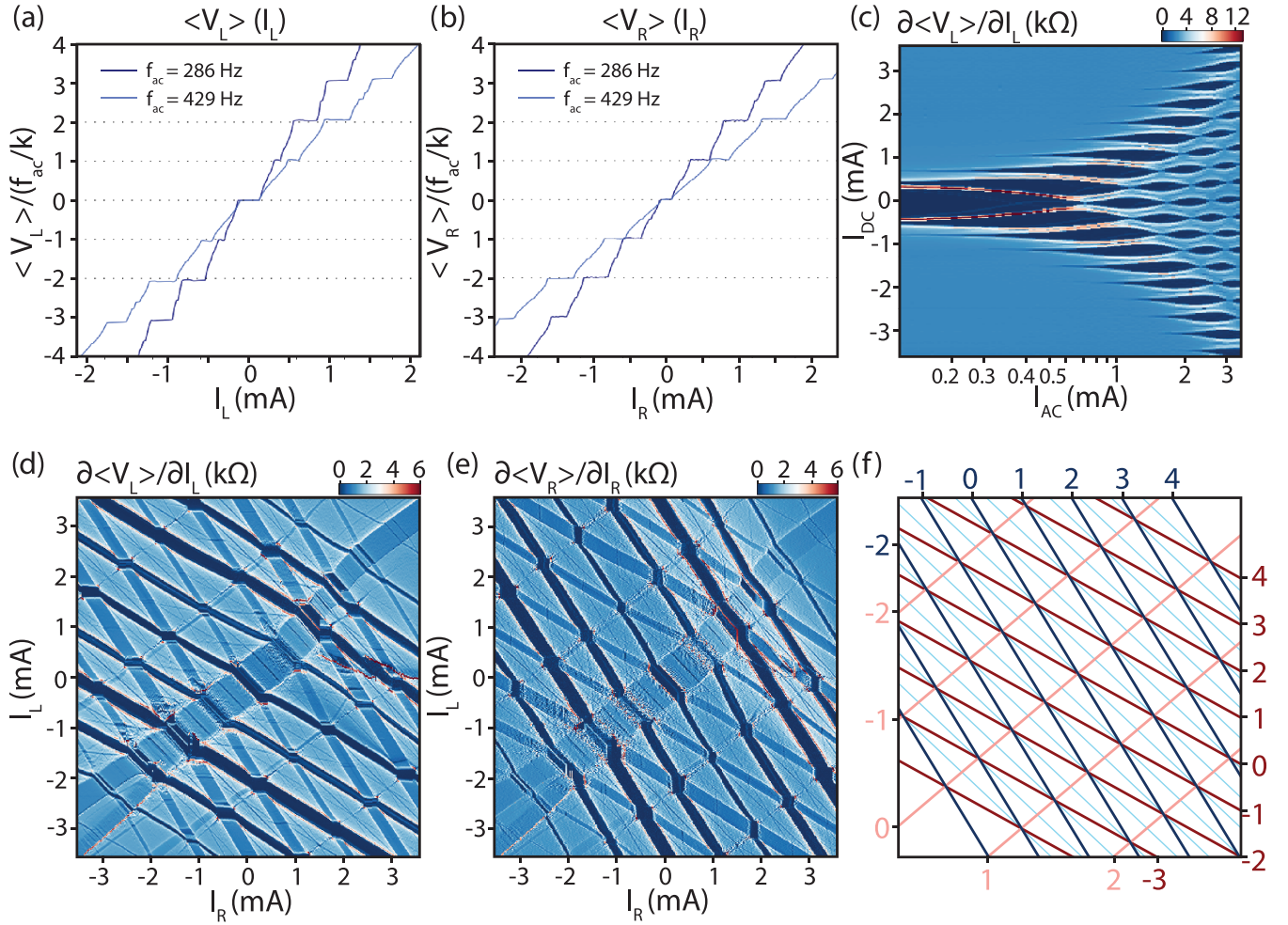
FIG. 2. (a) Shapiro steps in an AC driven uncoupled analog junction. $\langle V_L \rangle$ is plotted as a function of bias when $I_{ac} = 1.84$ mA and $f_{ac} = 429.2$ Hz (light blue), or $I_{ac} = 1.13$ mA and $f_{ac} = 286.7$ Hz. The junction voltage is expressed in units of the voltage quantum f_{ac}/k, which is why the slope of the trace changes despite the unchanged quality factor. (b) Shapiro steps for $\langle V_R \rangle$ using the same parameters. (c) Differential resistance $\partial\langle V_L \rangle/\partial I_L$ in the absence of coupling as a function of DC and AC biases at $f_{ac} = 286.7$ Hz. (d) Shapiro steps in the presence of transverse coupling. Differential resistance $\partial\langle V_L \rangle/\partial I_L$ as a function of both biases V_L and V_R. The map was measured with $f_{ac} = 429.2$ Hz and $I_{ac} = 1.76$ mA. (e) Differential resistance of the other channel $\partial\langle V_R \rangle/\partial I_R$ as a function of both biases I_L and I_R. (f) Schematic of the main resonances to notice in panels (d) and (e). Integer plateaus in $\langle V_L \rangle$ are labeled in dark red, plateaus in $\langle V_R \rangle$ are labeled in dark blue, plateaus in the transverse junction voltage $\langle V_L \rangle / - \langle V_R \rangle$ are labeled in pink, and quartet plateaus in $\langle V_L \rangle + \langle V_R \rangle$ are labeled in light blue.

similar plateaus were reported in Ref. [23] but have yet to be properly characterized in real three-terminal devices.

V. FRACTIONAL PHASE LOCKING

Maps of multiterminal Shapiro steps are only this simple when the junctions are sufficiently overdamped. Indeed, when the quality factor of the junctions is increased, additional fractional phase locked steps are observed. Fractional Shapiro steps can easily be seen even in single junctions with a sinusoidal CPR [25] but can also result from the interaction of two junctions within a network [4]. The measurement scheme is identical to what was discussed in the previous section. Figs. 3(a) and 3(b) show the same differential resistances $\partial\langle V_L \rangle/\partial I_L$ and $\partial\langle V_R \rangle/\partial I_R$ for a slightly underdamped analog junction network with a larger quality factor of ≈ 0.8. Plateaus are visible in both channels at integer phase locking for each

junction, similar to what was described in Fig. 2. However, new plateaus emerge at fractional multiples of the voltage quantum f_{ac}/k. These are visible as smaller stripes of vanishing differential resistance which for example can be seen around $(I_R = -1.4$ mA, $I_L = 1.1$ mA) for Fig. 3(a) and around $(I_R = -1.2$ mA, $I_L = 1.3$ mA) for Fig. 3(b). To gain insights into those patterns, we plot a cross section of $\langle V \rangle(I_R)$ along a Shapiro step of $\langle V_L \rangle$, indicated by a yellow dashed line in Fig. 3(a). We observe robust plateaus in $\langle V_R \rangle$ at fractional values with denominators up to five. Similarly, Fig. 3(d) corresponds to a cross section at constant $\langle V_R \rangle$ along the full yellow line indicated in panel B. The cross section shows fractional steps in $\langle V_L \rangle$

Note that fractional steps in $\langle V_L \rangle$ are only observed when $\langle V_R \rangle$ is integer phase locked, the converse being also true. For example, the fractions highlighted in Fig. 3(c) are obtained on top of the $n = 1$ plateau of $\langle V_R \rangle$. This implies that integer
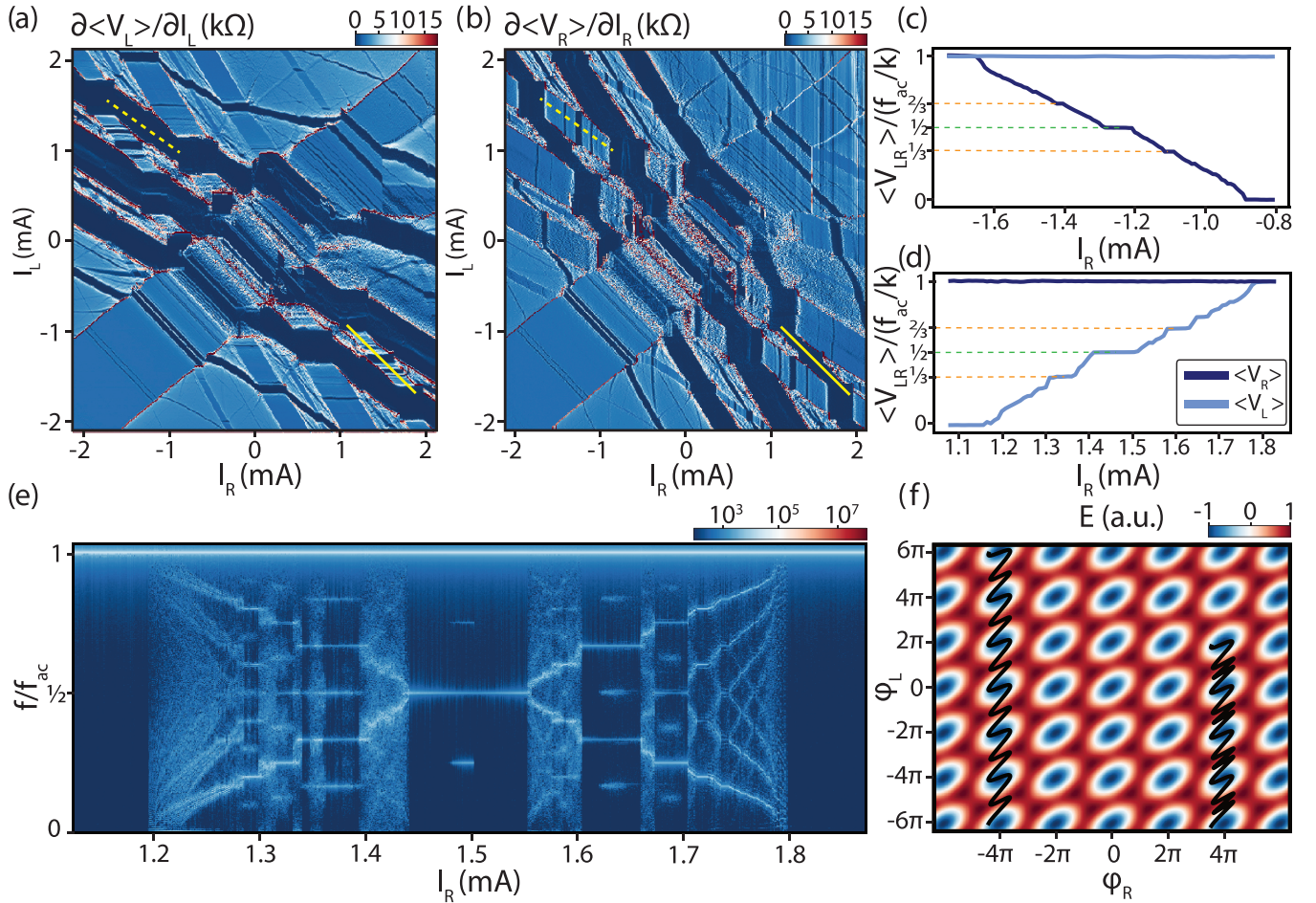
FIG. 3. AC fractional Shapiro steps in a driven analog junction network. (a) Differential resistance $\partial\langle V_L\rangle/\partial I_L$ as a function of both biases I_L and I_R. The map was measured with $f_{ac} = 687.7$ Hz and $V_{ac} = 1.2$ mA. (b) Differential resistance of the other channel $\partial\langle V_R\rangle/\partial I_R$. (c) Cross section $\langle V_L\rangle$ and $\langle V_R\rangle$ through a fractional Shapiro steps sequence as a function of I_R. The corresponding cross section is shown in yellow dashes on panel (a). It corresponds to an integer plateau of $\langle V_L\rangle$ which coincides with a sequence of fractional steps in $\langle V_R\rangle$. (d) Similar cross section, corresponding to the continuous yellow line in panel (a), where $\langle V_R\rangle$ is quantized and $\langle V_L\rangle$ goes through a sequence of fractional steps. (e) Frequency spectrum of $V_L(t)$ as a function of bias along the cross section shown in panel (a) by the bold yellow line. (f) Potential profile of the three-terminal junction. Two simulated trajectories in phase space are overlaid on top of the map, and each correspond to 12 cycles of the drive. The trajectory on the left corresponds to plateaus $\langle V_R\rangle = 0$ and $\langle V_L\rangle = \frac{1}{2}\frac{f_{ac}}{k}$, while the one on the right corresponds to $\langle V_R\rangle = 0$ and $\langle V_L\rangle = \frac{1}{3}\frac{f_{ac}}{k}$.

phase locking of one of the phases tends to stabilize fractions in the other channel.

We now turn to a time-domain analysis of the phase when fractional Shapiro steps are observed. We first record the unfiltered $V_L(t)$ and $V_R(t)$ at each bias value, then compute the fast Fourier transform in order to determine their frequency spectrum. We can then generate a map of that frequency spectrum along a bias cross section [25]. Figure 3(e) shows the spectral weight of the fast Fourier transform (FFT) as a function of frequency and bias, when the bias is evolving along the diagonal shown in Fig. 3(a). The main resonance in the frequency spectrum is of course the fundamental excitation frequency f_{ac} observed at 687.7 Hz. We see that whenever the I-V curve of the time filtered $\langle V_L\rangle$ shows a fractional Shapiro step, the frequency spectrum of the unfiltered $V_L(t)$ has stable subharmonics at f_{ac}/q, where q is the denominator of the fraction. This type of frequency spectrum is reminiscent of

what is observed in a single analog junction in the presence of fractional Shapiro steps [25].

To understand this behavior, as well the origin of the fractional steps, we turn to numerical simulations of the trajectories in phase space under different bias conditions. Details of those simulations are available in the Supplemental Material [31]. Figure 3(e) shows a map of the washboard potential, which if we drop a multiplicative constant can be written as $U(\varphi_L, \varphi_R) \propto -I_{cL}\sin(\varphi_L) - I_{cR}\sin(\varphi_R) - I_{cT}\sin(\varphi_L - \varphi_R)$. We plot two simulated trajectories of the phase over 12 cycles of the drive, and shift them by multiples of 2π to fit in this window. They correspond to φ_R in the $n = 0$ phase locked state, while φ_L is in the $n = 1/2$ (left) or $n = 1/3$ (right) phase-locked state. In both cases φ_R does not drift and just rocks back and forth. In the $n = 1/2$ case, we see that, at every other oscillation of the drive, the phase oscillates either across a minimum of the washboard potential
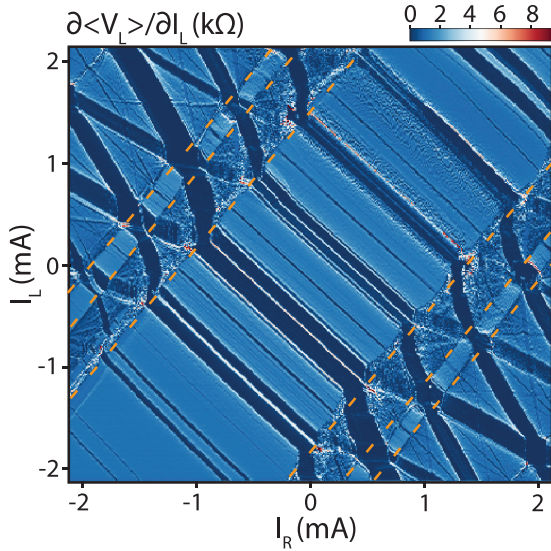
FIG. 4. Differential resistance $\partial \langle V_L \rangle / \partial I_L$ as a function of both biases I_L and I_R. The map was measured with $f_{ac} = 286.7$ Hz and $I_{ac} = 1.8$ mA. The effective transverse critical current was increased by a factor of 2.5 for this measurement, by dropping R_{T2} from 7.5 kΩ to 3 kΩ.

or along the saddle point between two maxima. Those two types of oscillations differ in amplitude, which explains the period doubling of the signal. In the $n = 1/3$ case, the phase oscillates twice along the saddle point and once across a minimum of potential, thus explaining the period tripling observed in Fig. 3(d). In both cases, oscillations around an otherwise unstable saddle point are dynamically stabilized by the rocking of φ_R. While fractional Shapiro steps can be observed in a single current-driven junction, our simulations strongly suggest that the fractional steps we observe are instead caused by the two-dimensional nature of the washboard potential for a three-terminal junction. This mechanism is reminiscent of the dynamical stabilization of classical multiplet supercurrents observed in Ref. [23], which was shown to be mathematically equivalent to Kapitza's inverted pendulum problem. This also explains the need for a larger quality factor to observe such fractions, since inertia facilitates this stabilization [23].

VI. SYNCHRONIZATION

Finally, we turn to the impact of transverse coupling on the synchronization of the two phases. To that end, we increase the value of the transverse coupling I_{cT}, which can just be done by reducing R_{T2}. We then measure the differential resistance $\partial \langle V_L \rangle / \partial I_L$, which is shown in Fig. 4. The map of $\partial \langle V_R \rangle / \partial I_R$ is essentially identical.

We focus in this section on the three stripes of suppressed differential resistance going from the bottom-left to top-right

corners of the map and whose boundaries are highlighted with orange dashed lines. These correspond to the quantization of the voltage across the transverse junction with $n = -1, 0, 1$. In those regions, the stability contours of the plateaus of $\langle V_L \rangle$ and $\langle V_R \rangle$ are identical because the two voltages are locked to each other by the quantization of the transverse junction. This explains why the slope of those plateaus changes as they intersect with plateaus of the transverse junction. We can also see that when the three types of stripes intersect, all three junctions are phase locked to an integer multiple of f_{ac}/k. This occurs for example around $I_L = 1$ mA, $I_R = -1$ mA, which corresponds to quantized voltages $\langle V_L \rangle = -2f_{ac}/k$, $\langle V_r \rangle = -f_{ac}/k$, and $\langle V_L - V_R \rangle = -f_{ac}/k$.

Note that, in a conventional Josephson junction a voltage quantum is $hf_{ac}/2e$, whereas in the analog equivalent it is f_{ac}/k, where k is the voltage to frequency gain of the junction. It is therefore important to calibrate the gain of the three VCOs so they are as close to each other as possible. We fine tuned them so that $k_L = 1817$ Hz/V, $k_R = 1818$ Hz/V, and $k_T = 1818$ Hz/V. Despite this calibration, we observe some artifacts that are caused by the nonuniversal size of Shapiro steps. These are most visible on top of the $n = 0$ plateau of the transverse junction, when it intersects plateaus of the other two junctions. These correspond to dark blue bands of slope ≈ -1 perpendicular to the widest plateau of slope ≈ 1. We see that each plateau splits into two in that region, which is barely noticeable in a voltage map, but striking in a differential resistance map.

Our results provide a convenient tabletop alternative to pure numerical modeling to observe and classify dynamical phenomena in multiterminal junctions. The low cost of the setup also makes it suitable to develop advanced undergraduate labs focusing on analog electronics and nonlinear dynamics. Although these results can be replicated using a fourth-order Runge-Kutta numerical scheme, the analog circuit offers a different approach to the problem. Its versatility makes it possible to vary most RCSJ circuit parameters, and visualize their impact on the overall phase dynamics in real time. Additionally, the characterization of the circuit uses electronic measurement techniques that are similar to what is used in typical low-temperature transport, which makes it easier to interpret transport measurements on real multiterminal devices, and to single-out quantum effects from dynamical ones.

[1] E. Strambini, S. D'Ambrosio, F. Vischi, F. S. Bergeret, Y. V. Nazarov, and F. Giazotto, The ω-SQUIPT as a tool to phase-engineer Josephson topological materials, Nat. Nanotechnol. **11**, 1055 (2016).

[2] Y. Cohen, Y. Ronen, J.-H. Kang, M. Heiblum, D. Feinberg, R. Mélin, and H. Shtrikman, Nonlocal supercurrent of quartets in a three-terminal Josephson junction, Proc. Natl. Acad. Sci. USA **115**, 6991 (2018).

[3] A. W. Draelos, M.-T. Wei, A. Seredinski, H. Li, Y. Mehta, K. Watanabe, T. Taniguchi, I. V. Borzenets, F. Amet, and G. Finkelstein, Supercurrent flow in multiterminal graphene Josephson junctions, Nano Lett. **19**, 1039 (2019).

[4] E. G. Arnault, T. F. Q. Larson, A. Seredinski, L. Zhao, S. Idris, A. McConnell, K. Watanabe, T. Taniguchi, I. Borzenets, F. Amet, and G. Finkelstein, Multiterminal inverse AC Josephson effect, Nano Lett. **21**, 9668 (2021).

[5] N. Pankratova, H. Lee, R. Kuzmin, K. Wickramasinghe, W. Mayer, J. Yuan, M. G. Vavilov, J. Shabani, and V. E. Manucharyan, Multiterminal Josephson Effect, Phys. Rev. X **10**, 031051 (2020).

[6] G. V. Graziano, J. S. Lee, M. Pendharkar, C. J. Palmstrøm, and V. S. Pribiag, Transport studies in a gate-tunable three-terminal Josephson junction, Phys. Rev. B **101**, 054510 (2020).

[7] K. Huang, Y. Ronen, R. Mélin, D. Feinberg, K. Watanabe, T. Taniguchi, and P. Kim, Interference of Cooper quartet Andreev bound states in a multi-terminal graphene-based Josephson junction, Nature Commun. **13**, 3032 (2022).

[8] R.-P. Riwar, M. Houzet, J. S. Meyer, and Y. V. Nazarov, Multi-terminal Josephson junctions as topological matter, Nat. Commun. **7**, 11167 (2016).

[9] E. Eriksson, R.-P. Riwar, M. Houzet, J. S. Meyer, and Y. V. Nazarov, Topological transconductance quantization in a four-terminal Josephson junction, Phys. Rev. B **95**, 075417 (2017).

[10] J. S. Meyer and M. Houzet, Nontrivial Chern Numbers in Three-Terminal Josephson Junctions, Phys. Rev. Lett. **119**, 136807 (2017).

[11] H.-Y. Xie, M. G. Vavilov, and A. Levchenko, Topological Andreev bands in three-terminal Josephson junctions, Phys. Rev. B **96**, 161406(R) (2017).

[12] H.-Y. Xie, M. G. Vavilov, and A. Levchenko, Weyl nodes in Andreev spectra of multiterminal Josephson junctions: Chern numbers, conductances, and supercurrents, Phys. Rev. B **97**, 035443 (2018).

[13] V. Fatemi, A. R. Akhmerov, and L. Bretheau, Weyl Josephson circuits, Phys. Rev. Res. **3**, 013288 (2021).

[14] B. Douçot, R. Danneau, K. Yang, J.-G. Caputo, and R. Mélin, Berry phase in superconducting multiterminal quantum dots, Phys. Rev. B **101**, 035411 (2020).

[15] R. Mélin, R. Danneau, K. Yang, J.-G. Caputo, and B. Douçot, Engineering the Floquet spectrum of superconducting multiterminal quantum dots, Phys. Rev. B **100**, 035450 (2019).

[16] K. Wiesenfeld, P. Colet, and S. H. Strogatz, Synchronization Transitions in a Disordered Josephson Series Array, Phys. Rev. Lett. **76**, 404 (1996).

[17] D. M. Abrams and S. H. Strogatz, Chimera States for Coupled Oscillators, Phys. Rev. Lett. **93**, 174102 (2004).

[18] S. Nichols and K. Wiesenfeld, Ubiquitous neutral stability of splay-phase states, Phys. Rev. A **45**, 8430 (1992).

[19] S. H. Strogatz and R. E. Mirollo, Splay states in globally coupled Josephson arrays: Analytical prediction of Floquet multipliers, Phys. Rev. E **47**, 220 (1993).

[20] M. Tinkham, *Introduction to Superconductivity*, 2nd ed. (Dover, Mineola, New York, 1996).

[21] D. McCumber, Effect of ac impedance on dc voltage-current characteristics of superconductor weak-link junctions, J. Appl. Phys. **39**, 3113 (1968).

[22] W. Stewart, Current-voltage characteristics of Josephson junctions, Appl. Phys. Lett. **12**, 277 (1968).

[23] E. G. Arnault, S. Idris, A. McConnell, L. Zhao, T. F. Q. Larson, K. Watanabe, T. Taniguchi, G. Finkelstein, and F. Amet, Dynamical Stabilization of Multiplet Supercurrents in Multiterminal Josephson Junctions, Nano Lett. **22**, 7073 (2022).

[24] R. L. Kautz, Noise, chaos, and the Josephson voltage standard, Rep. Prog. Phys. **59**, 935 (1996).

[25] A. McConnell, S. Idris, B. Opatosky, and F. Amet, Phase locking and noise-driven dynamics in a Josephson-junction electronic analog, Phys. Rev. B **104**, 184513 (2021).

[26] A. Melo, V. Fatemi, and A. R. Akhmerov, Multiplet supercurrent in Josephson tunneling circuits, SciPost Phys. **12**, 017 (2022).

[27] J. H. Magerlein, Accurate Josephson junction analog, Rev. Sci. Instrum. **49**, 486 (1978).

[28] C. A. Hamilton, Analog simulation of a Josephson junction, Rev. Sci. Instrum. **43**, 445 (1972).

[29] D. D'Humieres, M. R. Beasley, B. A. Huberman, and A. Libchaber, Chaotic states and routes to chaos in the forced pendulum, Phys. Rev. A **26**, 3483 (1982).

[30] J. A. Blackburn, Circuit for precision simulation of a capacitive Josephson junction, J. Appl. Phys. **101**, 093908 (2007).

[31] See Supplemental Material at http://link.aps.org/supplemental/10.1103/PhysRevB.106.174509 for additional details on the VCO, the derivation of the phase dynamics equation, as well as numerical simulations of the differential resistances.

[32] S. Shapiro, Josephson Currents in Superconducting Tunneling: The Effect of Microwaves and Other Observations, Phys. Rev. Lett. **11**, 80 (1963).

[33] T. F. Q. Larson, L. Zhao, E. G. Arnault, M.-T. Wei, A. Seredinski, H. Li, K. Watanabe, T. Taniguchi, F. Amet, and G. Finkelstein, Zero crossing steps and anomalous Shapiro maps in graphene Josephson junctions, Nano Lett. **20**, 6998 (2020).